Journal of Sound and Vibration 329 (2010) 3041–3064

Contents lists available at ScienceDirect

Journal of Sound and Vibration

journal homepage: www.elsevier.com/locate/jsvi

A waveguide finite element aided analysis of the wave field on a stationary tyre, not in contact with the ground

Patrick Sabiniarz *, Wolfgang Kropp

Division of Applied Acoustics, Chalmers University of Technology, SE 41296 Göteborg, Sweden

ARTICLE INFO

Article history:
Received 23 February 2009
Received in revised form
2 February 2010
Accepted 3 February 2010
Handling Editor: A.V. Metrikine
Available online 2 March 2010

ABSTRACT

Although tyre/road noise has been a research subject for more than three decades, there is still no consensus in the literature as to which waves on a tyre are mainly responsible for the radiation of sound during rolling. Even the free vibrational behaviour of a stationary (non-rotating) tyre, not in contact with the ground, is still not well understood in the mid- and high-frequency ranges. Thus, gaining an improved understanding of this behaviour is a natural first step towards illuminating the question of which waves on a rolling tyre contribute to sound radiation. This is the topic of the present paper, in which a model based on the waveguide finite element method (WFEM) is used to study free wave propagation, on a stationary tyre, in the range 0–1500 Hz. In the low-frequency region (0–300 Hz), wave propagation is found to be rather straightforward, with two main wave-types present. Both have cross-section modes involving a nearly rigid motion of the belt. For higher frequencies (300–1500 Hz) the behaviour is more complex, including phenomena such as 'curve veering' and waves for which the phase speed and group speed have opposite signs. Wave-types identified in this region include (i) waves involving mainly sidewall deformation, (ii) belt bending waves, (iii) a wave with significant extensional deformation of the central belt region and (iv) a wave with a 'breathing' cross-section mode. The phase speed corresponding to found waves is computed and their radiation efficiency is discussed, assuming free-field conditions. In a future publication, the tyre model will be used in conjunction with a contact model and a radiation model to investigate the contribution of these waves to radiated sound during rolling.

1. Introduction

Although at first glance a tyre might give the impression of a simple and somewhat trivial structure, on closer inspection it turns out to be far from easy to understand. The combination of geometrical properties, together with its multi-layer composite structure, leads to highly complex vibrational behaviour. Although tyre modelling has been a research topic for more than three decades, there is still no consensus in the literature as to which waves are responsible for the radiation of sound during rolling. Even the free vibrational behaviour of a stationary (non-rotating) tyre, not in contact with the ground, is still not well understood in the mid- and high-frequency ranges. Thus, gaining a clearer picture of this behaviour is a natural first step towards an understanding of the contribution of various waves to the sound radiation from a rolling tyre.

* Corresponding author. Tel.: +46 317722197.
E-mail address: patrick.sabiniarz@chalmers.se (P. Sabiniarz).

0022-460X/$ - see front matter © 2010 Elsevier Ltd. All rights reserved.
doi:10.1016/j.jsv.2010.02.008

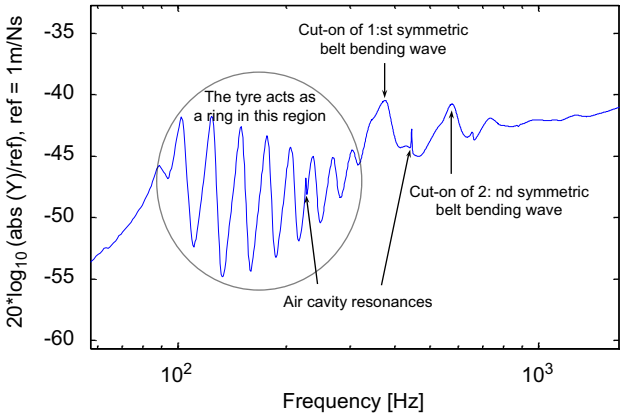

Fig. 1. Measured radial point mobility on a 'slick' tyre construction, with the exciting force placed at the tread centre-line. The sharp peaks located around 225 and 450 Hz, not commented upon in the text, are fluid resonances inside the air cavity.

In order to briefly review some of the existing knowledge on the vibrational behaviour of tyres, consider the radial point mobility depicted in Fig. 1. At low frequencies, below some 300 Hz, this quantity reveals the first modes responding in the radial direction. These modes result from interference of waves travelling along the positive and negative circumferential directions, with cross-section vibration patterns involving a nearly rigid radial displacement of the belt. For this reason, in this frequency range, a description of the tyre in terms of a ring (representing the belt) supported by elastic springs (representing the sidewalls) is justified. Typically, the elastic belt parameters play a minor role in this range, so that the main parameters are the pretension, the sidewall stiffness and the tyre weight per unit length. In addition, the apparent damping is relatively low. This range also involves a strong coupling between radial and tangential motion, due to the tyre's circumferential curvature. At the ring-frequency (around 400 Hz for a typical tyre), an in-plane wave cuts on, and well above this frequency in-plane and out-of-plane waves are more or less uncoupled.

Slightly below 400 Hz in Fig. 1, a wave cuts on for which the cross-section mode involves significant belt bending deformation. This event, which is manifested by a broad peak, marks the beginning of a region where wave propagation along both lateral and circumferential directions is present. Thus, the tyre exhibits 'tube-like' rather than 'ring-like' behaviour. As frequency increases further, higher-order belt bending waves cut-on, again manifested by broad peaks (two are visible at 580 and 740 Hz in Fig. 1). In this region, the flexural stiffness is dominating and the apparent damping is high as compared to the low-frequency range. The effect of pretension is not insignificant, however, since the cut-on frequency of waves is highly influenced by the lateral pretension.

At high enough frequencies, the wavelengths in both circumferential and lateral directions become small as compared to the tyre curvature along these directions. Consequently, the tyre behaves like a flat construction. Measurements of wave speed show an increase proportional to the square root of the frequency [1], as expected for bending waves on a plate. The high level of damping, combined with short wavelengths, ensures that waves travelling from the excitation position are virtually damped out before reaching this position again. The point mobility, therefore, approaches that of an infinite plate, which is given by a constant value (this behaviour is observed in the range 800–1300 Hz in Fig. 1).

Above some 1300 Hz in Fig. 1, the point mobility is seen to have an increasing trend. This is explained by the fact that the tread rubber around the excitation point exhibits high levels of local deformation. This phenomenon is highly dependent on the area over which the force is applied to the tread, as well as on the tread modulus. The smaller the excitation area and the lower the modulus, the more local deformation is induced. Further information on this topic can be found in [2].

The picture described in the above text is based on experimental work, as well as on simplified tyre models. These simplified models, although able to explain the measured driving point mobility well, do not consider the correct waves with respect to wave speed and cross-section mode. A correct description of the wave field is, however, essential for the investigation of sound radiation from tyres. It will be shown in this paper that besides the group of flexural-like waves (denoted by Group I henceforth) and the in-plane waves (denoted by Group II) a third group of waves exists in the frequency range below 1500 Hz. The question arises which of these groups of waves is responsible for the radiation of sound during rolling.

Generally, there are two ideas explaining which waves on a rolling tyre are responsible for the radiation of sound. Kim and Bolton [3] suggested that fast waves, identified as in-plane waves (belonging to Group II), are 'potential significant radiators at higher frequencies'. They especially pointed out the wave involving a breathing motion at the cross-section plane as driving the radiation. However, a proof of their theory is missing, since for the radiation of sound from a rolling tyre, forced vibrations are relevant rather than the free vibrations on which their reasoning was based.

Kropp et al. [4] investigated the radiation efficiency, σ, of modes on a cylinder in two dimensions and suggested that the low-order modes are the most efficient radiators. In the case of a rolling tyre, due to the forced vibration condition,

low-order modes are present also at higher frequencies and although their vibration amplitudes might be much smaller than the amplitudes of modes corresponding to the frequencies of interest, their σ is considerably higher.

Wullens and Kropp [5] used a contact model to calculate the dynamic contact forces on a rolling tyre and studied the resulting velocity field, along the tread centre-line, in Eulerian coordinates. The contribution of each 'rotating mode' to the total radiated sound power was analysed using a 2-D radiation model based on the equivalent source method. By considering the cumulative contribution of low-order modes belonging to Group I, it was found that a limited number are enough to accurately predict the total radiated power. This would simply mean that it is the variation over time of the contact patch geometry which leads to the radiated sound. One should bear in mind, however, that the results obtained in [5] were based on a radiation model, as well as tyre model, having simplified character. This especially refers to the tyre model, based on the assumption of a plate geometry. Such a model neglects the coupling between tangential and radial motion and therefore phenomena such as 'breathing modes' are not well represented.

In an attempt to investigate which waves on a rolling tyre are responsible for sound radiation, an appropriate first step is to gain a clear understanding of the types of waves that propagate on a typical tyre construction, along with their phase speeds. To undertake this first step is the aim of the present study, whereas the question of sound radiation from waves on a rolling tyre will be the subject of future publications. For this purpose, this work uses an in-house implementation of the model presented in [6, Paper A], based on the waveguide finite element method (WFEM), to study free wave propagation on a tyre that is (A) stationary and (B) not exhibiting contact with the ground. This model is described in detail and validated towards measurements in Section 2. This section also contains a review of some of the tyre models presented in the open scientific literature. Further, Section 3 describes the two types of dispersion diagram considered in this paper. The first type is obtained as the solution to an eigenvalue problem, whereas the second type is a frequency–wavenumber spectrum of the tyre displacement due to a point force. Section 4 focuses on identifying the different wave-types present in these diagrams, whereas in Section 5 the phase speed of found waves is computed and their radiation efficiency, assuming free-field conditions, is briefly discussed.

2. A model for the analysis of tyre vibration

2.1. Review of existing tyre models

Since the mid-1960s, a variety of different models have been developed, aiming at simulating the dynamic response of tyres. They range from analytical models, based on coarse simplifications of the geometrical and material properties, to highly sophisticated numerical models, accounting for the detailed physical properties of tyres. Generally, models belonging to the latter category, although flexible, suffer from high requirements on computer capacity and need for detailed input data. Those belonging to the opposite side of the spectrum, although simple and fast, have large restrictions in their modelling possibilities. In the following, a selection of tyre models found in the open scientific literature is reviewed.

One of the first models developed was that presented by Böhm in [7], where the tyre belt was described as a pretensioned ring, resting on a Winkler bedding. The bedding represents the sidewalls and the enclosed air cavity, whereas the pretension force is due to the inflation pressure. The model captures the dynamic behaviour below some 300–400 Hz, but fails above this frequency as wave propagation across the width of the belt starts to occur (as mentioned in Section 1). For this reason, Kropp [8] suggested an orthotropic plate model, accounting for both circumferential and lateral wave propagation. Again, the effect of support by the sidewalls and the pressurised air were taken into account by means of a set of isolated springs and pretension forces. Although the model neglects the curvature of the tyre, modelled mobilities compare surprisingly well with measured ones even in the low-frequency regime. A refined version of this model, which in addition to the features included by Kropp also takes the circumferential curvature into account, was used in [3]. Further, Muggleton et al. [9] presented a model consisting of an assembly of orthotropic plates, forming a straight tyre having 'U-shaped' cross-section.

As mentioned in Section 1, the point mobility on a tyre typically shows an increasing trend at higher frequencies, due to high levels of local deformation exhibited by the tread layer. This phenomenon, which is of large importance for the mechanical interaction between tyre and road, was first incorporated into a tyre model by Larsson and Kropp [10]. The suggested model describes the tyre as two coupled elastic layers forming a plate-like geometry, with the bottom layer representing the belt and the top layer the tread. The air cavity and sidewalls were accounted for in a manner similar to that described in the above paragraph. An extension of this model was later made in [11], where the local stiffening of the tread surface (which is due to gluing a plate to this surface) and the mass loading present in measurements of tyre responses were accounted for.

The rapid development of computer capacity during recent decades has made it possible to perform detailed modelling of tyres using the finite element method (FEM). A number of examples are found in the literature, of which a few are mentioned in the following. Kung et al. [12] investigated the difference in free response of a tyre with fixed and free wheel. Richards [13], by means of an FE-aided analysis including structural–acoustic coupling, computed the tread surface vibration response and force transmission to the hub, due to a force applied to the tread. Pietrzyk [14] modelled the same quantities, using a somewhat refined model, whereas Fadavi et al. [15] dealt with the free and forced response of a rolling

tyre in contact with a flat rigid substrate. The response of rotating tyres, making contact with the ground, was also modelled by Brinkmeier et al. in [16] and by Lopez et al. in [17].

Waki et al. [18] presented a model based on an approach by which the tyre is considered as a waveguide along the circumferential direction. The concept is to first model a short section of the waveguide using standard finite elements. A periodicity condition is then applied, stating that the displacements at one end of this section are related by an exponential function to the displacements at the other end (the same condition is imposed on forces acting at the section ends). An eigenvalue problem results from which the dispersion properties and cross-section modes are obtained for all waves found by the model. Nilsson [19] developed a model based on the waveguide finite element method (WFEM), an approach related to that described above in the sense that it also makes use of an FE technique to model the response of waveguides. The model considers the structural as well as fluid domain, using waveguide finite elements of the thin shell type, fluid type and fluid–structure coupling type.

A modified version of the model in [19] has also been presented in [6, Paper A], where thick shell elements were used to model the sidewalls and belt and solid elements to model the tread (details on the formulation behind these elements can be found in [20]). An additional difference as compared to [19] is that the air cavity was excluded. The model described in [6, Paper A], with one simplification introduced, has also been implemented by the authors and is used for the analysis conducted in Section 4. For this reason, the remainder of this section is devoted to describing this model, starting by reviewing some fundamentals of the WFEM as well as some of the references concerned with it.

2.2. The waveguide finite element method

Structures, fluids or combined fluid/structure systems, having constant physical properties along a single direction, are often referred to as 'waveguides'. This stems from the fact that from a mathematical point of view, the considered field can be described in terms of a set of waves along this direction. The WFEM, as the name implies, is an FE-based approach by which approximate wave solutions are found for such structures or fluids. More specifically, the method uses a 2-D FE model over the cross-section of the waveguide in order to arrive at a set of coupled partial differential equations, to which source-free solutions have the physical interpretation of waves. The approach is very versatile, as it applies to virtually any 'object' falling within the above definition of a waveguide, examples including fluid-filled pipes and 'slick' car tyres.

For increased clarity, consider the straight rod in Fig. 2 (a), for which the cross-section geometry and material parameters are assumed constant along the X-direction. Due to this assumption, each displacement component in this figure (u_X, u_Y and u_Z) can be separated into one factor dependent on the cross-section coordinates (Y and Z) and a second factor dependent on the X-coordinate and time (X and t). The basic concept of the WFEM is to prescribe, for each

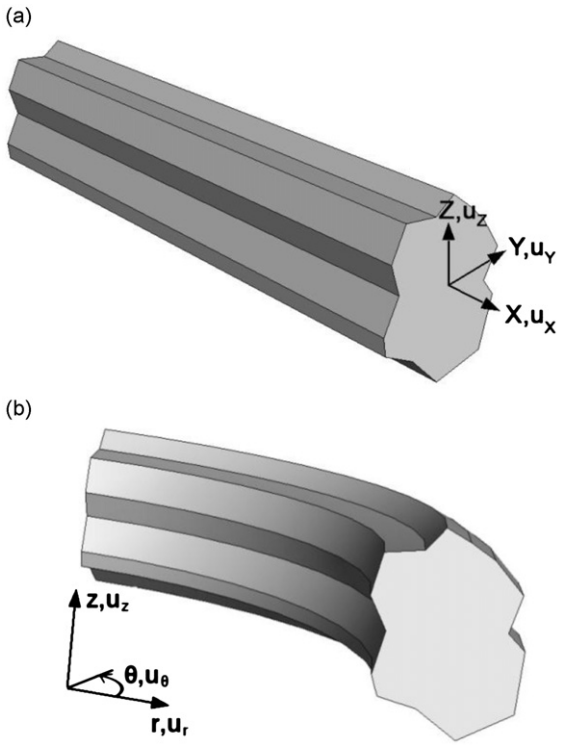

Fig. 2. (a) Straight rod with waves along the X-axis. (b) Curved rod with waves along the θ-direction.

displacement component, FE shape functions for the dependence on the cross-section coordinates only. Consequently, nodal degrees of freedom (dof) are functions of the X-coordinate and time. To summarise

$$u_i(X,Y,Z,t) = \underbrace{f_i(Y,Z)\cdot g_i(X,t)}_{\text{Factorization of } u_i} \approx \underbrace{\mathbf{N}_i(Y,Z)\cdot \mathbf{U}_i(X,t)}_{\text{FE-approximation of } u_i} \qquad i = X,Y,Z \tag{1}$$

In the above relation $\mathbf{N}_i(Y, Z)$ is a vector with each entry given by a shape function, whereas $\mathbf{U}_i(X, t)$ contains an equal number of nodal dof. By means of the approximation in Eq. (1) and by use of FE procedures, the approximate equations of motion arrived at, Eq. (2), are a set of coupled partial differential equations (for details on the procedures leading from Eq. (1) to (2), the reader may refer to [20]). The stiffness matrices $\mathbf{K}_i$ and mass matrix $\mathbf{M}$ in this relation stem from the potential and kinetic energies of the structure, respectively, whereas $\mathbf{F}(X, t)$ is a vector originating from the external load. Further, $\mathbf{V}(X, t)$ contains all nodal dof in the model.

$$\left[\mathbf{K}_2\frac{\partial^2}{\partial X^2} + \mathbf{K}_1\frac{\partial}{\partial X} + \mathbf{K}_0 + \mathbf{M}\frac{\partial^2}{\partial t^2}\right]\mathbf{V}(X,t) = \mathbf{F}(X,t) \tag{2}$$

In the absence of external loads, the right-hand side in Eq. (2) vanishes and a general solution for $\mathbf{V}(X, t)$ is then written in terms of an eigenvector together with an exponential function: $\mathbf{V}(X, t) = \boldsymbol{\psi} e^{j(kX-\omega t)}$. This solution has the physical interpretation of a wave travelling along the X-direction, with cross-section mode $\boldsymbol{\psi}$, angular frequency ω and wavenumber k. By substitution of this general solution into the homogenous form of Eq. (2), an eigenvalue problem results, Eq. (3), from which the dispersion properties and cross-section modes are obtained for all waves 'captured' by the model. For means of dealing with forced response problems, involving a non-vanishing right-hand side, the reader is directed to [19].

$$[-k^2\mathbf{K}_2 + jk\mathbf{K}_1 + \mathbf{K}_0 - \omega^2\mathbf{M}]\boldsymbol{\psi} = \mathbf{0} \tag{3}$$

If a curved waveguide was considered instead of a straight one, Eqs. (1)–(3) still apply after minor revision. The cylindrical coordinate system pertaining to a curved waveguide is given in Fig. 2 (b) where z is the axis of revolution, r is the radial direction and θ is the angle along the circumference. The latter coordinate is that along which wave propagation occurs, and the former two ones define the cross-section plane. By means of substituting X for θ, Y for r and Z for z in Eqs. (1) and (2), new relations describing the curved structure are obtained. It is stressed that the stiffness and mass matrices are different for a straight and curved waveguide and therefore the relation obtained from Eq. (2) after substitution only gives the new format of the wave equation for a curved structure. Similarly, substituting k for the polar wavenumber κ in Eq. (3) gives the new format of the eigenvalue problem for a curved waveguide.

The main advantage of the WFEM as compared to standard FE formulations is the decreased calculation burden. This stems from the fact that only the cross-section is discretized, reducing the number of dof introduced to the model. An additional advantage compared to conventional FE is that different wave-types are easy to identify and analyse, allowing for a somewhat deeper physical understanding of the investigated structure [6].

References concerned with the WFEM start with Aalami's work [21], where straight waveguide finite elements were derived for a solid domain having isotropic material properties. These elements were later used by Gavric [22] to study the type of propagating waves encountered on railway rails. Gavric [23] was also the first author to deal with thin-walled structures. Thin shell elements were formulated and used to study the free response of a cylindrical shell and a beam with 'I-shaped' cross-section. Orrenius and Finnveden [24] used the shell elements derived by Gavric to study propagating waves in rib-stiffened plate structures. Nilsson and Finnveden [25] also derived fluid elements and elements for fluid–structure coupling, which were used together with thin shell elements to model fluid-filled ducts. The latter author also used the WFEM to evaluate the modal density of a wind tunnel [26], which was used as input for a statistical energy analysis (SEA). Birgersson et al. [27] presented an approach, referred to as the 'super spectral element method', by which forced response solutions are found in a manner parallel to the 'wave approach' [28] used for beams and bars. It was also demonstrated how structures consisting of parts acting as waveguides, together with parts having more complicated properties, can be modelled by combining the WFEM and the regular FEM. Regarding tyre modelling, Refs. [19] and [6, Paper A] were already mentioned in sub-section 2.1. The model presented in [6, Paper A] has also been used in conjunction with contact models and radiation models for the computation of rolling resistance [6, Paper B] and sound radiation during rolling [29].

2.3. Implementation of the WFE-model

2.3.1. General description of the model

Although a tyre is a complicated mechanical system, in the absence of lateral tread layer grooves the cross-section geometry and material properties are constant along the circumferential direction. It is, therefore, possible to describe the response of a tyre in terms of a set of waves along this direction, which are modelled numerically using the WFEM. As stated previously, two models adopting this technique were developed in the past, described in [19] and [6, Paper A], respectively. The present study uses an in-house implementation of the model presented in [6], with the exception that the wheel is not considered, as discussed in the next paragraph.

Generally, including the wheel is of main interest when (A) the tread-to-hub force transmission is sought, or when (B) comparing modelled to measured tyre responses at low frequencies. The latter point stems from the fact that measurements on tyres are typically conducted on freely suspended tyre–wheel configurations, where low-frequency modes are strongly affected by the finite rim mass. Such conditions apply to the measured mobilities presented for validation purposes in sub-section 2.3.3. Beyond this, however, there is little motivation to include the rim in the present study and it is therefore neglected by simply blocking the tyre's motion at the beads.

Also worth mentioning within the context of a general model description is that the present model does not account for the air-filled cavity. This is motivated by the fact that modes found on the coupled fluid/structure system generally have either strong structural or strong acoustic character and are little affected by the coupling [13]. Thus, since the main interest of the present study lies in the modes on a tyre being predominantly structural, the fluid cavity is omitted. Worth mentioning, however, is that although generally weak, the coupling is sufficient to considerably affect the force transmission between tread and hub around the first fluid resonance. This is, presumably, the main motivation for including the air cavity in [19].

To sum up, with the exception that the rim is not considered, the model used by the authors describes the tyre in the same way as in [6, Paper A]. Thus, the sidewalls and belt were modelled in terms of thick shell elements, accounting for both rotational inertia and shearing across the element thickness. Pretension due to inflation and layered material properties were also incorporated into the element formulation. Displacements and rotations were interpolated locally using second-order polynomials, and for this reason the shell element used has three nodes. The tread layer was modelled by means of solid elements, having isotropic material properties and allowing for compression. Interpolation within the element was again quadratic, using a Lagrange type of element. The specific mesh used for the studies conducted in this paper, involving 46 shell elements and 20 solid elements, is given in Fig. 3 (each dot in this figure represents a node-line). In [29] Rustighi et al. reported that a mesh consisting of about 40% less structural elements (25 shell elements and 13 solid elements) was sufficient for analysis up to 1500 Hz. Thus, although this paper does not consider the same tyre structure as in [29], one expects the mesh in Fig. 3 to be sufficient at least up to the same frequency. This was confirmed by a small convergence study conducted by the authors.

As a last note it is mentioned that among the methods available for solving forced response problems (see [19] for an overview) the present paper uses the 'assumed modes procedure' explained in [6]. Briefly, the idea is to expand the response around the tyre circumference in terms of a Fourier series, with the Fourier coefficients obtained, at each frequency, from a linear system of equations.

2.3.2. Input data

The model requires as input, for each of the elements in Fig. 3, data specifying the elastic properties, pretension forces, inertia and damping. Most of the required input was obtained from an input deck provided by Continental, whereas the remaining data had to be found either by physical reasoning or from measured responses. In the following, the input data definition is briefly discussed.

The input deck describes the tread as an isotropic and homogeneous layer, so that the elastic properties are given in terms of two parameters: the Young's modulus E and Poisson's ratio ν. The latter assumes a constant value, about 0.49, whereas the former quantity is frequency-dependent. Specifically, data are provided in increments of 50 Hz, starting with 28 MPa at 100 Hz and increasing to 44 MPa at 1600 Hz. In Fig. 4 this modulus is used (together with the data described in paragraphs below) to compute the tangential point mobility (a quantity almost exclusively determined by the tread modulus and excitation area for frequencies above the resonance of the rotational semi-rigid body mode (schematically depicted on p. 29 in [6, Paper A]). The measured mobility is also given and, as seen, it is clearly underestimated in the simulation. It was found that a frequency-independent modulus of about 20 MPa yielded better agreement towards measurements, and for this reason this value has been used for all simulations presented henceforth.

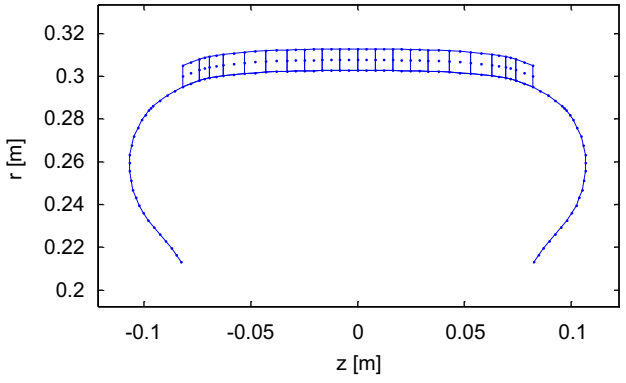

Fig. 3. Mesh used to model the Continental 205/55R16 tyre under investigation in this paper.

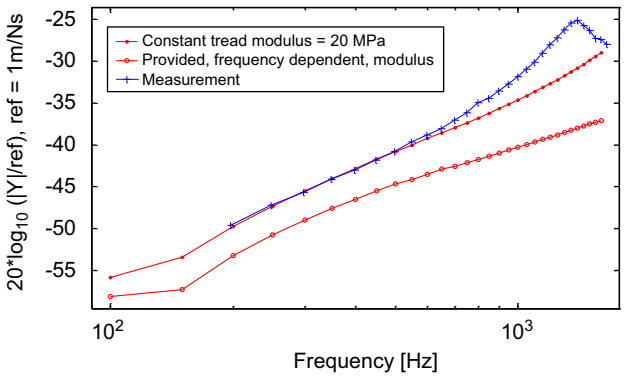

Fig. 4. Comparison between measured and modelled magnitude of the tangential point mobility. The force applied to the tread centre-line and the excitation area is $16 \times 16\,\mathrm{mm}^2$.

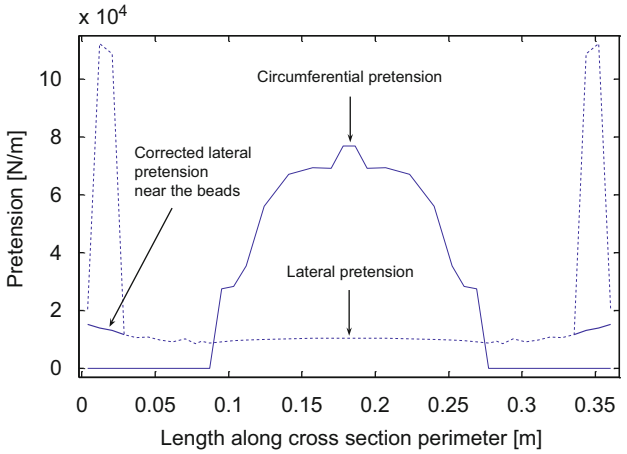

Fig. 5. Pretension due to inflation.

The sidewalls and belt were modelled as orthotropic shell elements, exhibiting no coupling between membrane forces and bending strains (or, equivalently, between bending moments and membrane strains). The corresponding elastic parameters, given by the input deck, are again frequency-dependent quantities in the range 100–1600 Hz. However, since this dependence is small, it has not been taken into account within the present study. Further, the input deck does not provide information on the two shear stiffness parameters describing shearing across the element thickness. Therefore, for each shell element, these two parameters were assigned the same value as the in-plane shear stiffness (a quantity given by the input deck), for lack of better estimates.

Data provided for the pretension forces, acting on the sidewalls and belt, are given in Fig. 5. As seen, the lateral force reaches very high values near the beads. This is an unphysical result, since for static equilibrium to prevail for a strip going around the tyre, the lateral pretension must be inversely proportional to the radius r in Fig. 3 [6, Paper A]. For this reason, this pretension component was corrected to more physically reasonable values as indicated in the figure.

In addition to the stiffness data discussed above and data provided for the density of all individual elements, dissipative properties had to be assigned. This was done in a somewhat simplified manner, assuming stiffness proportional damping, meaning that all stiffness parameters in the model (tread modulus, pretension and all elastic parameters for the shell elements) were assigned the same loss factor $\eta(\omega)$. Its value in the low-frequency range was first estimated from the 3 dB bandwidths of modes located at 125, 150 and 175 Hz in Fig. 1, resulting in an average of about η=0.05. Above the cut-on frequency of the first symmetric belt bending wave (see Fig. 1), the belt no longer deforms along the circumferential direction only—out-of-plane motion along both the lateral and circumferential directions is present. Since a large portion of the strain energy is stored in the tread for this type of motion, global damping is significantly increased as compared to lower frequencies. By comparing simulated results towards measurements, it was found that η=0.15 is an appropriate value in this frequency range. The frequency-dependent loss factor inserted to the model can, therefore, be summarised according to Fig. 6.

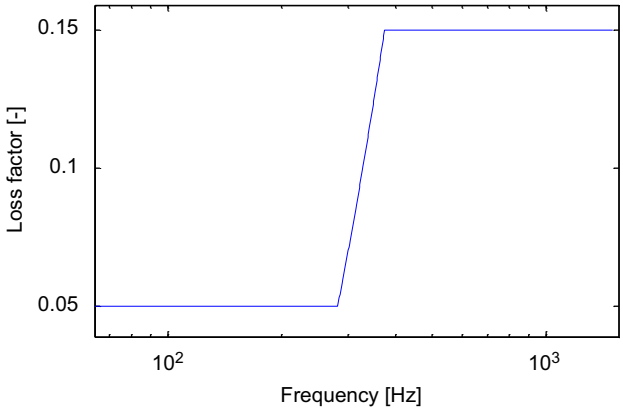

Fig. 6. Frequency-dependent loss factor.

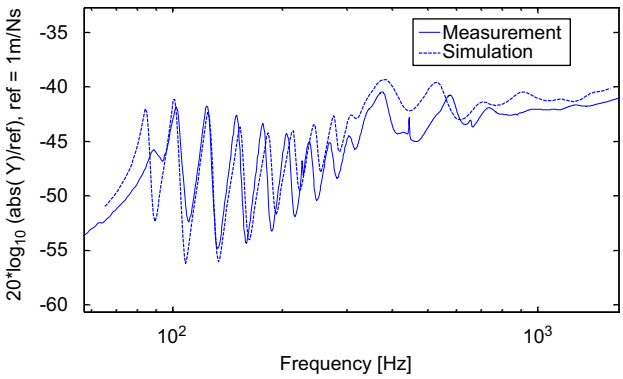

Fig. 7. Comparison between measured and modelled magnitude of the radial point mobility. The force is applied to the tread centre-line.

Using the input data discussed above, it was found that simulated responses were a bit stiff as compared to measured results. A slightly improved agreement was obtained by, in addition to the modifications described above, reducing the circumferential bending stiffness for all shell elements by 50% and the circumferential pretension by 25%. With this data tuning, modelled and measured responses are in good general agreement, as described in the following.

2.3.3. *Validation*

In order to validate the implemented model, simulated point and transfer mobilities were compared to the corresponding measured quantities. The measurements were conducted on a freely suspended tyre, due to the difficulties in realizing a clamped rim condition. Standard equipment was utilised, using a shaker (fed with band-limited white noise) as excitation and piezoelectric devices to pick up the input force and tyre response signals. A picture of the setup is found in [2].

A comparison between the simulated and measured point mobility is given in Fig. 7. In the low-frequency range, spanning from 0 to some 100 Hz, the measured response cannot be well reproduced by the model. The reason is that in this frequency region, the measured tyre is significantly affected by the finite rim mass and acts as a mass–spring–mass system. In the simulation, however, by blocking the tyre displacements at the beads, the rim mass is assumed infinite. Due to these differences, simulated results are not displayed over the first part of the low-frequency range.

The modes located between 100 and 300 Hz are seen to be fairly well predicted with respect to their natural frequencies. The same applies for the cut-on of the first symmetric belt bending wave, whereas the second and third symmetric belt bending waves have cut-on frequencies which are slightly underestimated by the model.

For frequencies above some 250 Hz, the modelled point mobility has a magnitude which is generally higher than that measured. The deviation is explained, partly, by different levels of local deformation in simulation and experiment. This statement is most easily verified by considering Fig. 8, where the measured and modelled real part of the point mobility is compared—a quantity which is highly insensitive to the amount of local deformation present (since the input power is not much affected by such deformation). As seen, above 250 Hz levels are in closer agreement than in Fig. 7, verifying the statement made above. The different levels of local deformation in simulation and experiment are, in turn, explained by differences in excitation. To be specific, in the measurement the load is applied onto a $16 \times 16\,\mathrm{mm}^2$ aluminium plate,

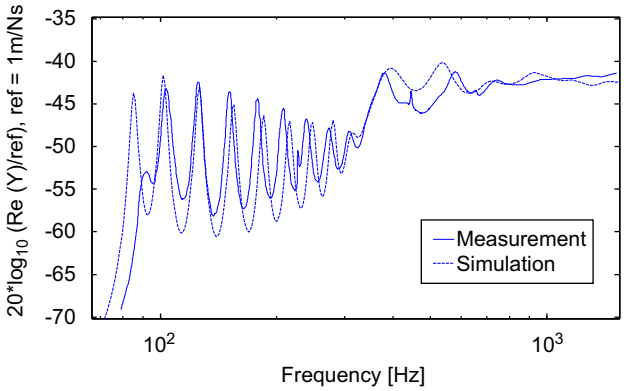

Fig. 8. Comparison between measured and modelled real part of the radial point mobility. The force is applied to the tread centre-line.

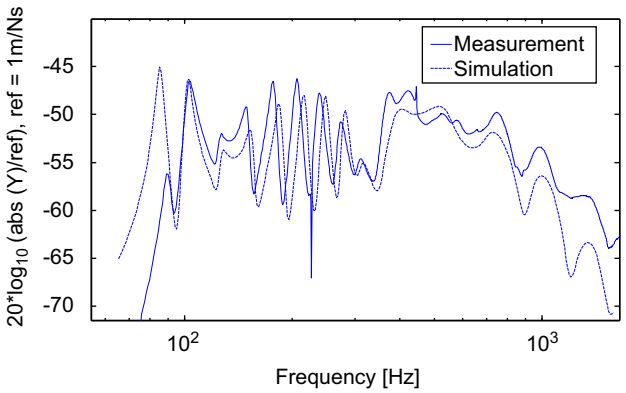

Fig. 9. Comparison between measured and modelled magnitude of the radial transfer mobility for 150 mm separation. Excitation and response points are located along the tread centre-line.

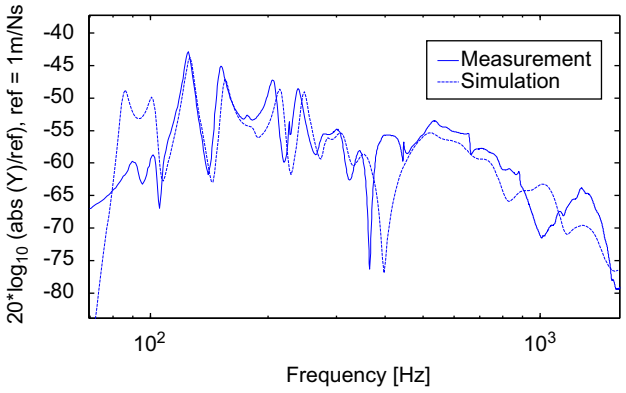

Fig. 10. Comparison between measured and modelled magnitude of the radial transfer mobility for 300 mm separation. Excitation and response points are located along the tread centre-line.

which is glued to the tyre. In the simulation, however, the load is given by a uniform pressure distribution (applied over an equal area), allowing for higher levels of local deformation.

In addition to the point mobility, Figs. 9–11 depict the transfer mobilities for separation distances of 150, 300 and 450 mm. Often a comparison between measured and modelled transfer responses is avoided, since a very high accuracy in amplitude and phase speed of waves is demanded for a good agreement. Here, however, a comparison is made to demonstrate the quality of the model.

Generally, below 400 Hz, results in Figs. 9–11 are in very good agreement, which is relatively easy to achieve, since wave propagation is only one-dimensional (1-D). Above this frequency, however, waves propagate in the lateral direction too and, as a consequence, interference phenomena between different waves reflected at the beads are visible. Positive

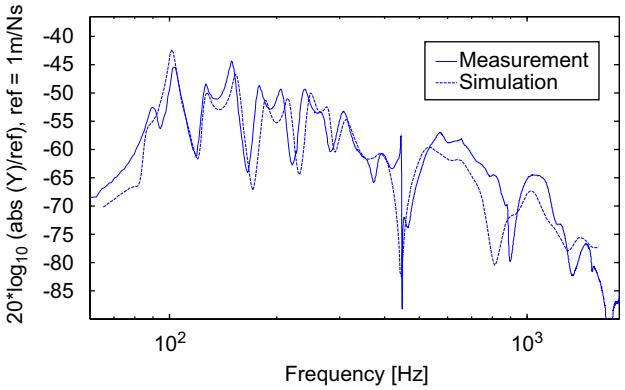

Fig. 11. Comparison between measured and modelled magnitude of the radial transfer mobility for 450 mm separation. Excitation and response points are located along the tread centre-line.

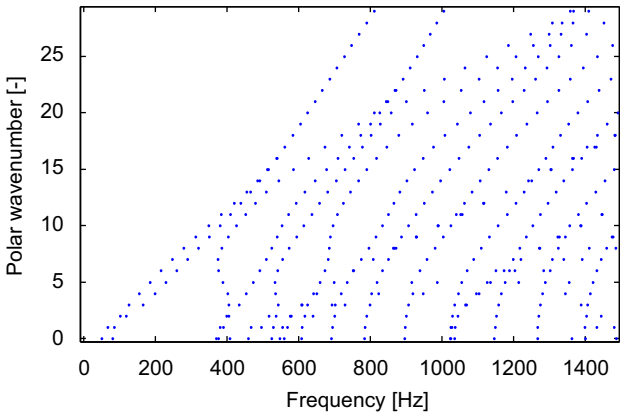

Fig. 12. Dispersion relations, assuming no damping. A frequency at which a dot is found corresponds to a natural frequency for the undamped tyre.

interference is manifested by broad maxima in the mobility, whereas negative interference leads to very distinct and sharp minima. Small deviations in the phase speed of waves will shift these minima in frequency, whereas amplitude deviations will lead to differences in the amount of negative interference. For the cases compared here, the agreement is rather good, indicating that both the amplitude and phase speed of waves are well predicted.

To sum up, measured and modelled results are in good general agreement, indicating that the implementation is correct and that the material data used are representative for the tyre under study.

3. Dispersion diagrams

A good way of obtaining an overview of the properties of different waves on a tyre is to consider its dispersion relations. These relations describe, for the different waves found by the model, how wavenumber is related to frequency. In this study, the focus is on propagating waves, and two types of dispersion diagram describing such waves are considered. In the following, they are briefly described.

The first type of diagram (A) is constructed by considering the eigenproblem in Eq. (4), describing free waves on a curved waveguide. This eigenproblem can be solved in two different ways, either by assuming a fixed frequency and treating the polar wavenumber as unknown or vice versa. The first approach leads to a quadratic eigenvalue problem in κ, whereas the second one result in a linear generalized eigenvalue problem in ω. If the interest is in the dispersion properties of propagating waves only, as in this work, the latter approach is typically preferred, since it evaluates considerably faster (for further details on this matter, see [26]). Thus, diagram (A) is here constructed by solving Eq. (4) several times, each time assuming a new real-valued wavenumber κ, and by marking the resulting frequency solutions $f_i(k)=(\omega_i^2(\kappa))^{1/2}/2\pi$ into a diagram (these are the frequencies of the propagating waves at wavenumber κ). If the tyre exhibits no damping, these frequencies are real-valued quantities. An example of a dispersion diagram constructed in this manner is given in Fig. 12, in which all $f_i(\kappa)<1500$ Hz are depicted for $\kappa=0$, $\kappa=1$, …, $\kappa=29$ (in Fig. 13 (a and b) this diagram is repeated, but with various symbols introduced to mark different groups of modes, see figure caption). It should be noted that Fig. 12 refers to wave propagation along the positive θ-direction only, since κ is positive and a propagation function of the form

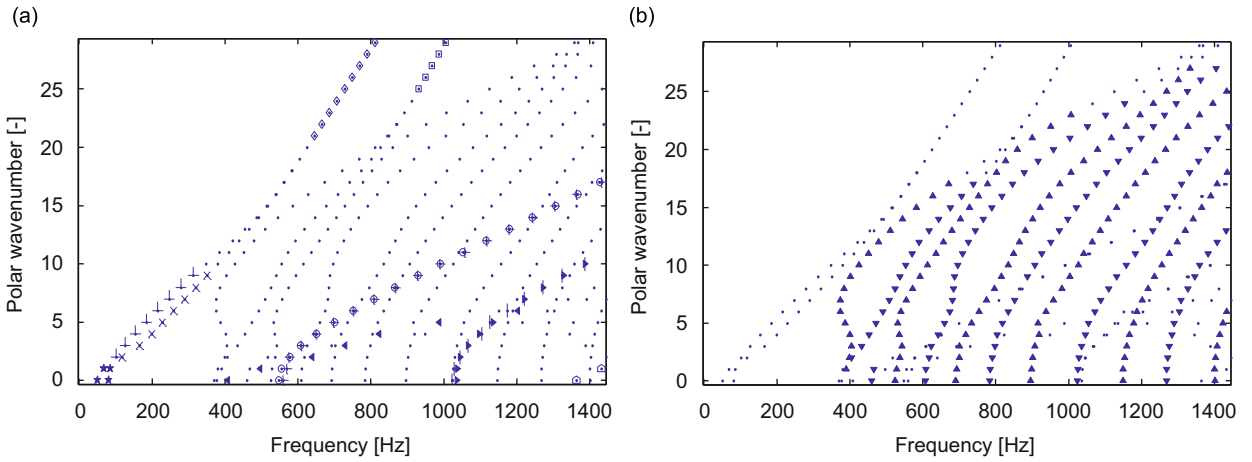

Fig. 13. (a) and (b). These figures are the dispersion relations in Fig. 12 repeated, but with various symbols introduced to mark different groups of modes. The symbols are explained in Section 4.

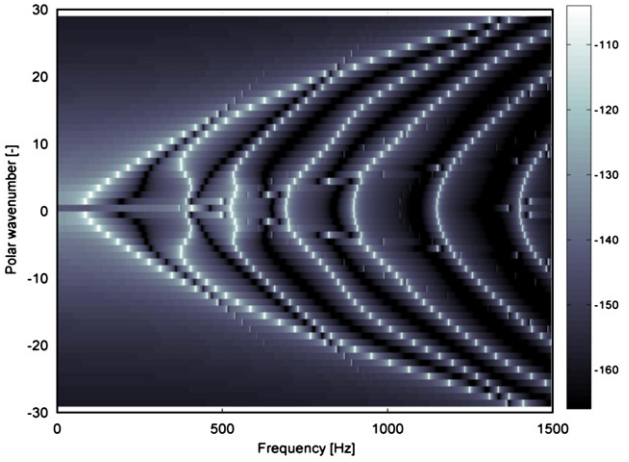

Fig. 14. Magnitude (in dB) of frequency–wavenumber spectrum. No damping assumed. Positive wavenumbers correspond to positive going waves and negative wavenumbers to negative going waves.

$e^{j(k\theta-\omega t)}$ is assumed. However, since the considered tyre is non-rotating, it holds that $f_i(\kappa)=f_i(-\kappa)$, so that the dispersion properties of negative going waves are obtained by simply mirroring each 'dot' in Fig. 12 against the frequency axis. Also worth noting is that since the tyre is a closed structure, natural frequencies are obtained when the polar wavenumber κ takes on an integer value (or, stated differently, when a whole number of free wavelengths fit along the tyre circumference). Thus, if a 'dot' is found at coordinate $(\overline{f},\overline{\kappa})$ in Fig. 12, then one of the tyre's natural frequencies is $\overline{f}$. Further, to this natural frequency corresponds a 3-D vibration pattern, which is obtained by combining the waveform corresponding to the 'dot', $\overline{\mathbf{\Psi}}$, with a motion along the circumference involving $\overline{\kappa}$ complete wavelengths. In conclusion, each 'dot' in Fig. 12 can be interpreted either as a 'sampling point' on one of the tyre's dispersion branches or as representing a natural frequency.

$$[-\kappa^2\mathbf{K}_2+j\kappa\mathbf{K}_1+\mathbf{K}_0-\omega^2\mathbf{M}]\Psi=\mathbf{0} \tag{4}$$

The second type (B) is essentially a frequency–wavenumber spectrum of the tyre displacement, when subjected to an external force. It is constructed by applying a radial point force to the tyre and computing the resulting radial response at equally spaced points along the complete circumference. Both excitation and response points are located along the tread centre-line. By means of an FFT, the sampled displacement is subsequently brought from the spatial domain to the wavenumber domain and, repeating this process for several frequencies, the spectrum is established. Examples, involving different amounts of damping, are given in Figs. 14–16. It should be noted that only waves which respond significantly to the exciting force are manifested in these figures. Thus, this type of diagram only identifies the waves on the tyre having a significant radial response along the tread centre-line.

To sum up, the first type of diagram, (A), displays the dispersion properties of *all* propagating waves found by the model, but does not provide information about the damping of these waves. The second type, (B), although providing information

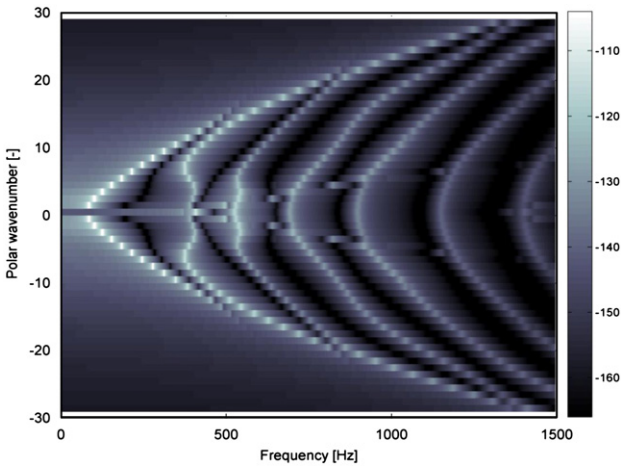

Fig. 15. Magnitude (in dB) of frequency–wavenumber spectrum. $\eta(\omega)$ in Fig. 6 has been divided by a factor 10. Positive wavenumbers correspond to positive going waves and negative wavenumbers to negative going waves.

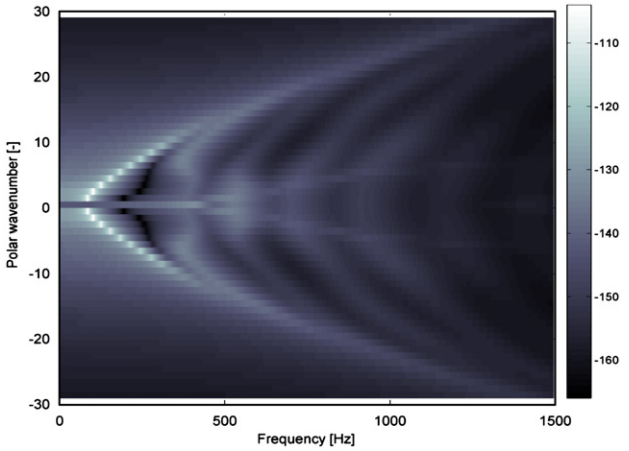

Fig. 16. Magnitude (in dB) of frequency–wavenumber spectrum. Damping according to Fig. 6. Positive wavenumbers correspond to positive going waves and negative wavenumbers to negative going waves.

on damping, only identifies the waves responding to the exciting force. By considering both types of diagram, understanding of wave propagation on the tyre is facilitated.

4. Analysis of dispersion diagrams

This Section aims at summarising some of the information provided by the dispersion diagrams in Section 3. Specifically, the focus is on identifying the different wave-types present in these diagrams, whereas the grouping of these waves, as well as their radiation efficiency, is discussed in Section 5. The analysis made is subdivided by considering the low-frequency (0–300 Hz) and high-frequency (300–1500 Hz) ranges separately. Main observations are summarised by the following set of points.

4.1. Low frequency range (0–300 Hz)

• To start with, consider the four lowest natural frequencies in Fig. 13 (a), marked by the symbol '★' (two correspond to $\kappa=0$ and the remaining ones to $\kappa=1$). The corresponding 3-D mode shapes are depicted in Figs. 17–20 and, as seen, these shapes represent semi-rigid body motion (note that pure rigid body motion is not possible in the model, since the tyre's motion at the beads has been blocked). Thus, for each of the four vibration patterns in Figs. 17–20, the belt acts as a rigid ring and the sidewalls as supporting springs. The first mode seen at $\kappa=0$ (Fig. 17) corresponds to a displacement of the rigid ring along the z-direction (the direction given by the axis of revolution). For this reason, it is referred to as a 'telescopic mode' in the literature. The second mode having zero-valued κ (Fig. 18) involves a rotation of the ring around the z-axis and is typically

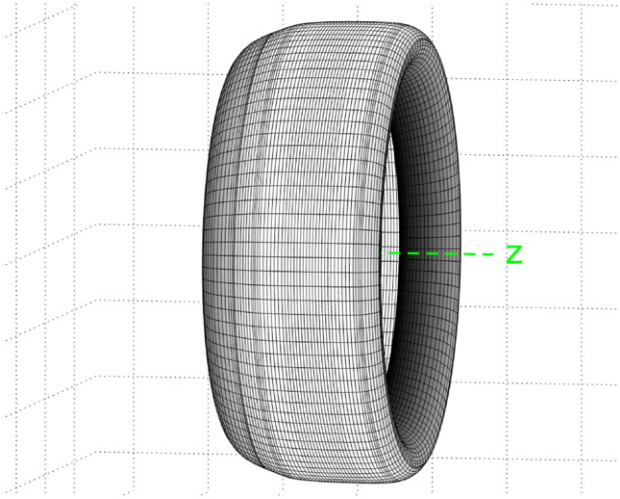

Fig. 17. 'Telescopic' semi-rigid body mode corresponding to $\kappa=0$ and $f=51$ Hz (symbol '★' in Fig. 13 (a)).

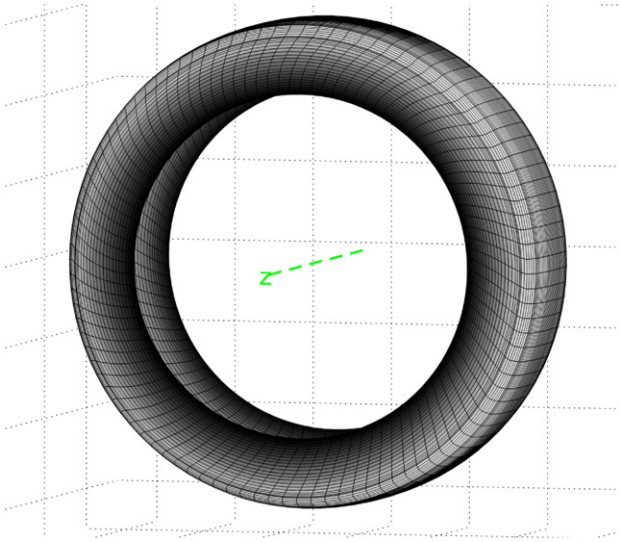

Fig. 18. 'Rotational' semi-rigid body mode, corresponding to $\kappa=0$ and $f=81$ Hz (symbol '★' in Fig. 13 (a)).

described as a 'rotational mode'. Continuing, the first mode encountered at $\kappa=1$ (Fig. 19) also involves a rotating motion of the ring, but around the radial axis r instead. It sometimes goes under the designation 'rocking mode'. Finally, the second mode at $\kappa=1$ (Fig. 20) is given by a displacement of the ring along the radial direction.

- The last mode mentioned in the above paragraph (see Fig. 20) is strongly excited by a radial force applied to the tread centre-line. Therefore, at its resonance frequency (around 85 Hz), it is clearly manifested in Figs. 14–16 as two strong wave components—the two wave components into which the 3-D mode can be decomposed. Both components have the cross section mode depicted in Fig. 21 and the first one corresponds to $\kappa=1$ (positive going) and the second one to $\kappa=-1$ (negative going). As frequency increases, additional resonances are created by the wave in Fig. 21, when a whole number of wavelengths fit along the tyre circumference. These resonances are given the symbol '$\perp$' in Fig. 13 (a) and, as seen, they are located along a nearly straight line. This indicates an almost linear wavenumber-to-frequency relation, so that the phase speed of this wave can be taken as a constant value.
- In the vicinity of the natural frequencies just discussed, another set of frequencies are observed, marked by the symbol '$\times$'. By closer inspection, they are found to correspond to a wave with cross-section mode according to Fig. 22. As seen, this waveform has an anti-symmetric character, involving a rotation of the belt. Since there is no radial response along the tread centre-line, this wave is not possible to detect in Figs. 14–16.

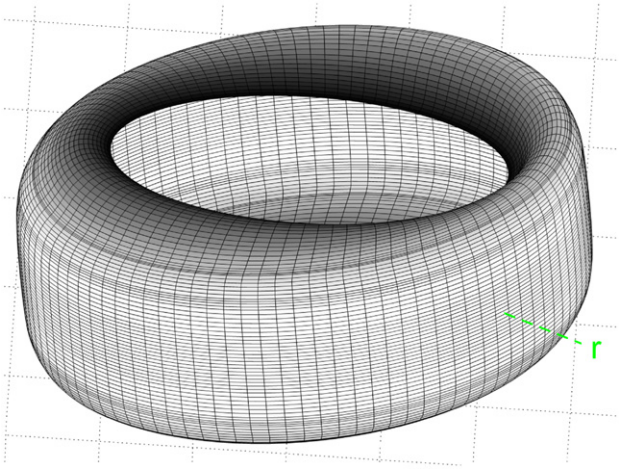

Fig. 19. 'Rocking' semi-rigid body mode, corresponding to $\kappa=1$ and $f=67$ Hz (symbol '★' in Fig. 13 (a)).

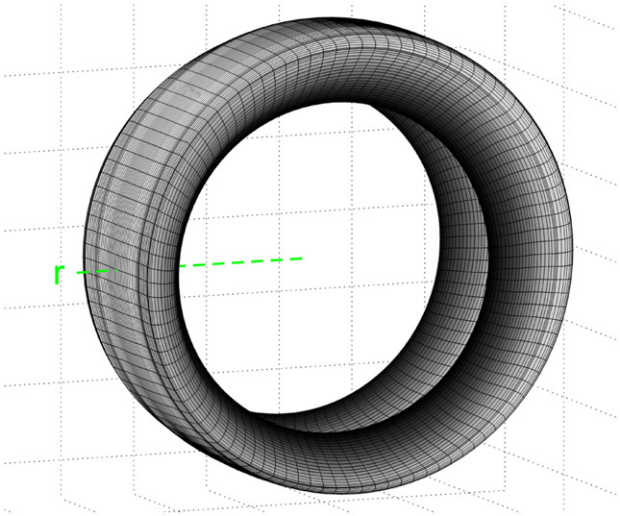

Fig. 20. Semi-rigid body mode, corresponding to $\kappa=1$ and $f=85$ Hz (symbol '★' in Fig. 13 (a)).

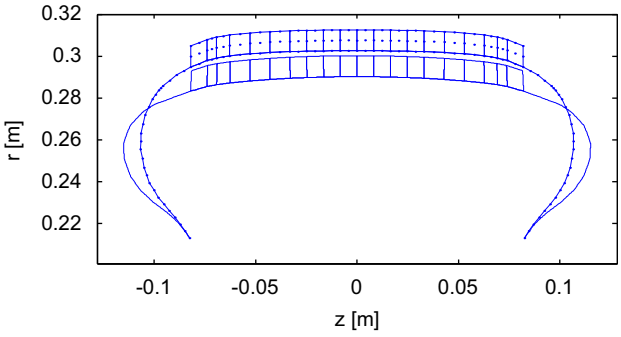

Fig. 21. Cross-section mode corresponding to $\kappa=3$ and $f=126$ Hz (symbol '⊥' in Fig. 13 (a)).

In summary, wave propagation on the tyre below some 300 Hz is rather straightforward, with two main wave-types ('⊥' and '×') present. Their cross-section modes involve a nearly rigid motion of the belt and have symmetric and anti-symmetric character, respectively (Figs. 21 and 22). These results are in agreement with the findings made in [6, Paper A].

4.2. High frequency region (300–1500 Hz)

• Above 370 Hz, a number of dispersion branches are observed in Fig. 14 corresponding to waves involving significant belt bending deformation. These branches are assigned the symbol '▲' in Fig. 13 (b) and the corresponding waveforms are symmetric. To be specific, for each such waveform, the number of half-wavelengths of out-of-plane displacement is an odd integer. This number is denoted by M henceforth and two examples depicting the $M=5$ and 7 cross-section modes are given in Figs. 23 and 24. These waveforms belong to the first and second '▲'-marked branches in Fig. 13 (b), respectively, when viewed from left to right.

As seen, over parts of the two branches just mentioned, a phenomenon is observed by which the natural frequencies decrease with increasing wavenumber (meaning a negative group speed). This phenomenon, which was also addressed in [18] and [30], does not apply to the higher-order belt bending waves, for which dispersion curves are seen to have more 'plate-like' character. As an example, following the leftmost '▲'-marked branch in Fig. 13 (b), for increasing wavenumber the natural frequencies go from increasing to decreasing to increasing again. Due to this behaviour, a large number of

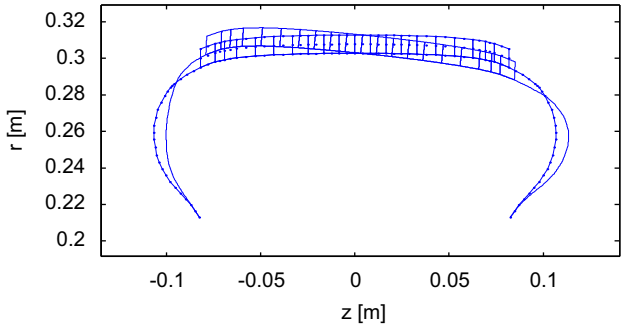

Fig. 22. Cross-section mode corresponding to $\kappa=3$ and $f=165$ Hz (symbol '×' in Fig. 13 (a)).

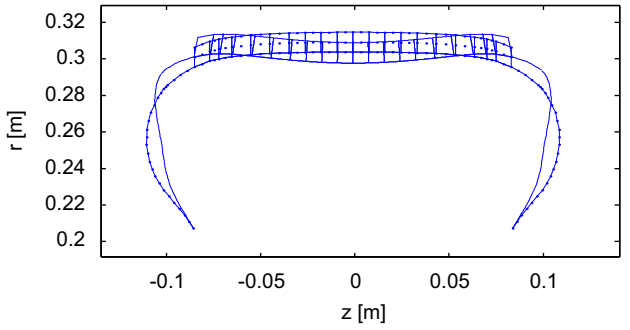

Fig. 23. Cross-section mode corresponding to $\kappa=8$ and $f=386$ Hz (symbol '▲' in Fig. 13 (b)). This waveform involves $M=5$ half-wavelengths of out-of-plane displacement.

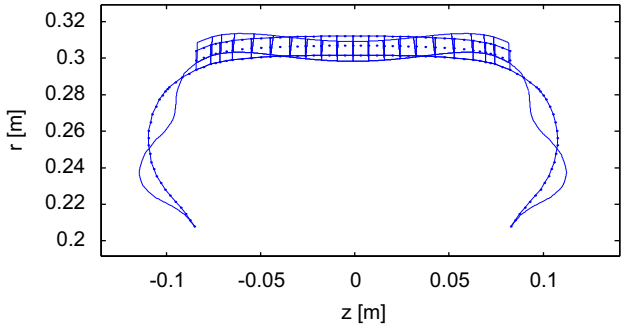

Fig. 24. Cross-section mode corresponding to $\kappa=8$ and $f=574$ Hz (symbol '▲' in Fig. 13 (b)). This waveform involves $M=7$ half-wavelengths of out-of-plane displacement.

resonances are found in the range 370–390 Hz and together with high damping this explains the height and broadness of the peak observed around 380 Hz in Fig. 7 (thick line).

In addition to the symmetric belt bending waves, a similar set of anti-symmetric waves also exist, corresponding to the symbol '▼' in Fig. 13 (b). Due to the anti-symmetry, the value of M belonging to each cross-section mode is now given by an even integer. Two examples involving M=6 and 8 are depicted in Figs. 25 and 26. These waveforms correspond to the first and second '▼'-marked branches (again, when viewed from left to right). Briefly, the dispersion branches representing anti-symmetric waves behave in a way similar to those representing symmetric waves.

• As seen in Fig. 13 (a), when the polar wavenumber increases beyond some κ=10, the branches discussed in subsection 4.1 ('⊥' and '×') approach each other. As this happens, the corresponding cross-section modes (Figs. 21 and 22) are gradually changed. To be specific, the relation between sidewall displacement and belt displacement increases, so that the waveforms are increasingly dominated by sidewall deformation. In the region $\kappa > 20$ the branches are more or less converged and the cross-section modes no longer change significantly with increasing κ. The symbol '◇' has been used in this region, with each '◇' enclosing two closely spaced 'dots'. As seen from Figs. 27 and 28, the cross-section modes now

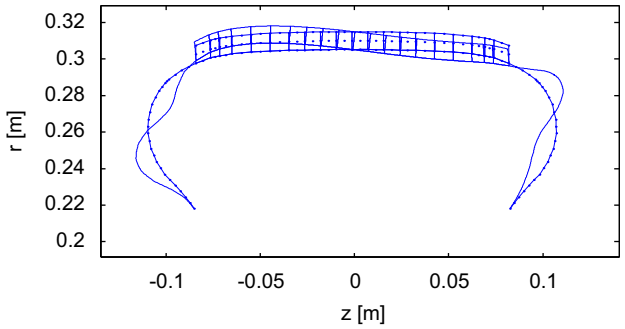

Fig. 25. Cross-section mode corresponding to κ=8 and f=525 Hz (symbol '▼' in Fig. 13 (b)). This waveform involves M=6 half-wavelengths of out-of-plane displacement.

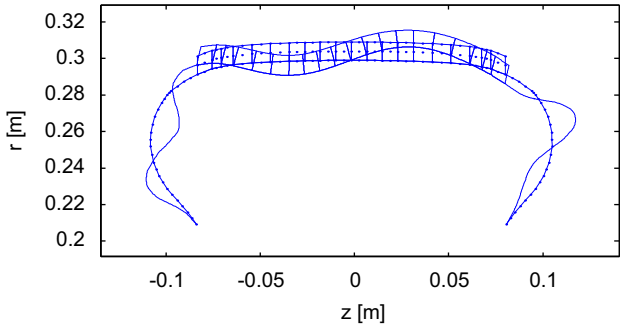

Fig. 26. Cross-section mode corresponding to κ=8 and f=685 Hz (symbol '▼' in Fig. 13 (b)). This waveform involves M=8 half-wavelengths of out-of-plane displacement.

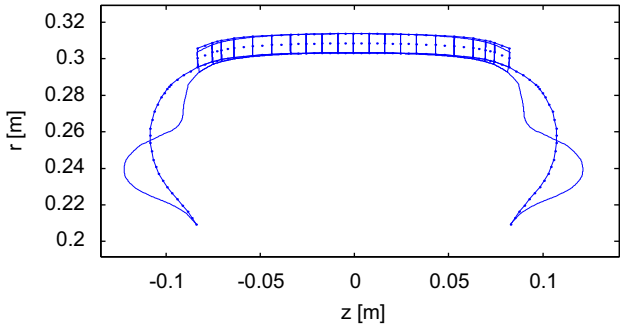

Fig. 27. Cross-section mode corresponding to κ=25 and f=727.450 Hz (symbol '◇' in Fig. 13 (a)).

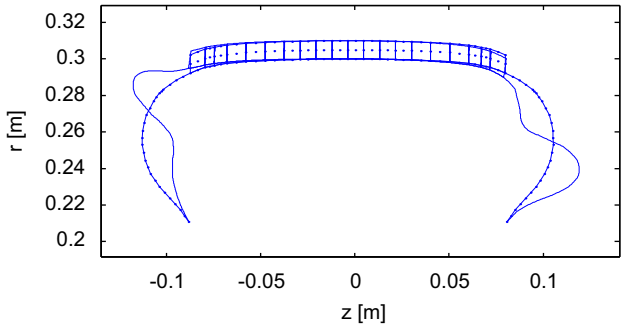

Fig. 28. Cross-section mode corresponding to $\kappa=25$ and $f=727.457$ Hz (symbol '◇' in Fig. 13 (a)).

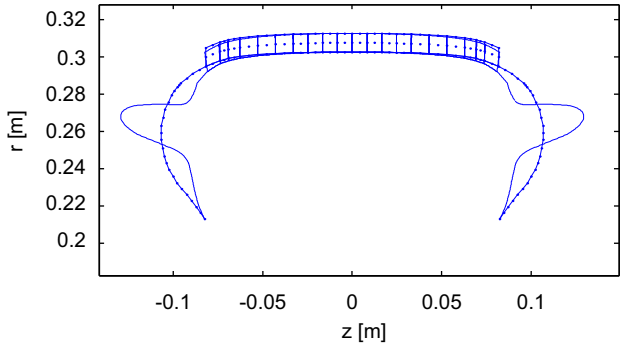

Fig. 29. Cross-section mode corresponding to $\kappa=29$ and $f=1004.61$ Hz (symbol '□' in Fig. 13 (a)).

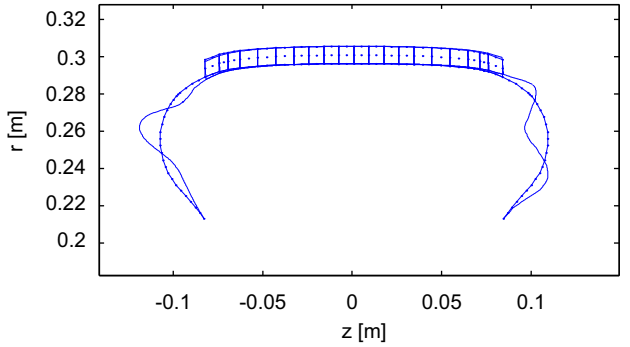

Fig. 30. Cross-section mode corresponding to $\kappa=29$ and $f=1004.62$ Hz (symbol '□' in Fig. 13 (a)).

have a strong 'sidewall character' and may be classified as 'sidewall modes'. To be specific, in these figures, one wavelength of out-of-plane displacement is observed at each sidewall, with the walls vibrating in phase (Fig. 27) and in anti-phase (Fig. 28), respectively.

In addition to the pair of sidewall waves just described, another pair with similar properties, but of higher order, is found at somewhat higher frequencies. This pair, which is assigned the symbol '□' in Fig. 13 (a) (each '□' encloses two 'dots'), 'emerges' from the $M=5$ and 6 belt bending waves. The corresponding waveforms are depicted in Figs. 29 and 30 and as seen, the motion at the cross-section plane now involves $\frac{3}{2}$ wavelengths of out-of-plane displacement at each sidewall. At increased frequencies, this phenomenon is repeated several times, with higher-order sidewall waves 'emerging' from higher-order belt bending waves (this, however, happens outside the frequency–wavenumber region depicted in the dispersion diagram). As a final note, it is observed that the branches given by the symbols '◇' and '□' are virtually straight, indicating a nearly constant phase speed.

• By close inspection of Fig. 14 wave cutting on near 560 Hz can be detected, assigned the symbol '+' in Fig. 13 (a). As seen from the latter figure, this wave exhibits a relatively high phase speed as compared to the belt bending waves.

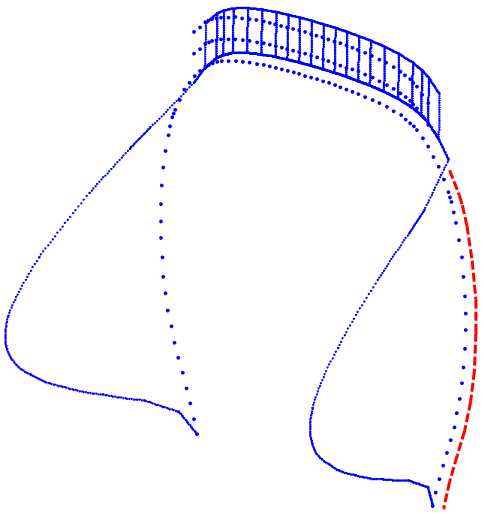

Fig. 31. Cross-section mode corresponding to $\kappa=0$ and $f=559$ Hz (symbol '+' in Fig. 13 (a)). The thick dashed line (extending from the bead to the shoulder) marks the lateral direction, as referred to in the third paragraph of sub-section 4.2.

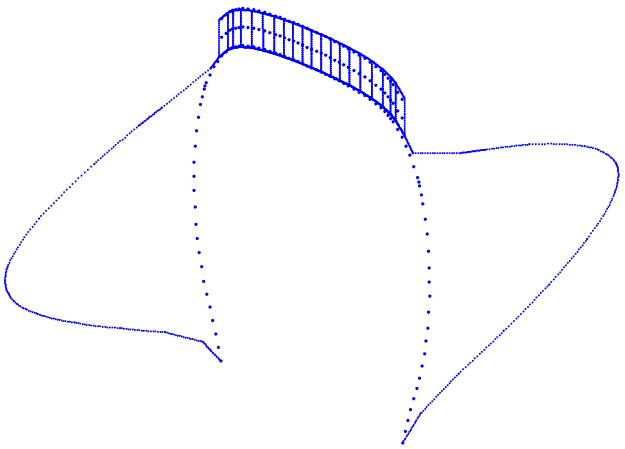

Fig. 32. Cross-section mode corresponding to $\kappa=0$ and $f=547$ Hz (symbol '○' in Fig. 13 (a)).

Further, inspecting the cross-section modes belonging to each '+' in Fig. 13 (a) reveals that this wave is characterized by large in-plane sidewall displacement, see Fig. 31. To be specific, when moving along the lateral direction of a sidewall (that is, when moving along the thick dashed line in Fig. 31), one half-wavelength of displacement along the θ-direction is observed. Also seen is that the depicted waveform is symmetric, with the sidewalls vibrating in phase.

The dispersion branch just discussed is closely followed by a branch marked '○' in Fig. 13 (a). The corresponding wave has properties similar to its 'neighbour', involving large in-plane sidewall displacement, as seen in Fig. 32. However, as opposed to the vibration pattern in Fig. 31, the sidewalls now vibrate in anti-phase, so that the considered waveform is anti-symmetric.

In addition to the addressed pair of waves, a pair with similar character, but of higher order, cuts on near 1030 Hz. These waves are assigned the symbols '|' and '▶' in Fig. 13 (a) and their waveforms are depicted in Figs. 33 and 34.

• Moving along the axis $\kappa=0$ in Fig. 14, a set of modes are observed involving zero wavelengths of displacement along the circumference. Each is referred to as a 'breathing mode', since the tyre's motion along the tread centre-line involves a uniformly growing (and contracting) shape. The first such mode is observed at 370 Hz and its motion at the cross-section plane is similar to that in Fig. 21, involving $M=3$ half-wavelengths of out-of-plane displacement. The five subsequent breathing modes, located between 400 and 1200 Hz, involve a successive increase in the number M. At some 1360 Hz, however, a mode is found with cross-section motion according to Fig. 35. As seen, this motion corresponds to $M=1$, so that

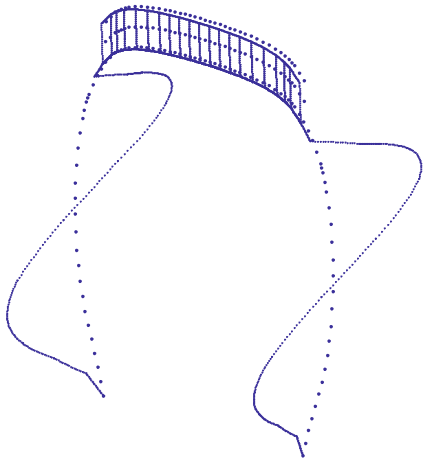

Fig. 33. Cross-section mode corresponding to $\kappa=0$ and $f=1023$ Hz (symbol '|' in Fig. 13 (a)).

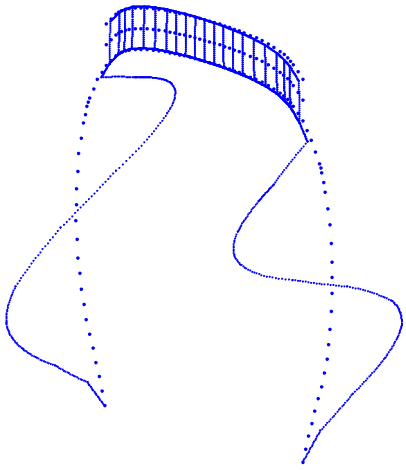

Fig. 34. Cross-section mode corresponding to $\kappa=0$ and $f=1036$ Hz (symbol '▶' in Fig. 13 (a)).

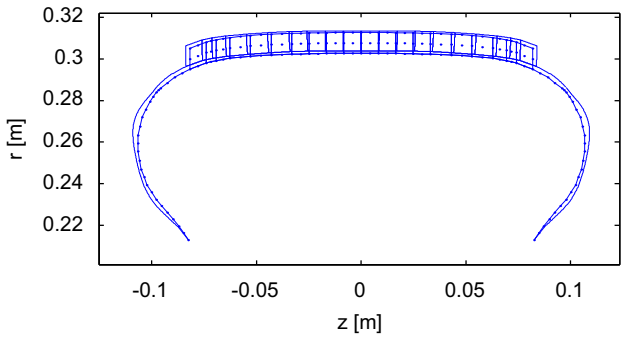

Fig. 35. Cross-section mode corresponding to $\kappa=0$ and $f=1363$ Hz (symbol '⌂' in Fig. 13 (a)).

the tyre exhibits a uniformly growing (and contracting) shape not only along the circumference, but at the cross-section plane too. This mode marks the cut-on of a wave, symbol '⌂' in Fig. 13 (a), with a relatively high phase speed as compared to the belt bending waves and with a 'breathing' waveform. Worth noting is that the rather high cut-on frequency of this wave (as compared to the cut-on of other waves involving a low M, for example $M=4$ (Fig. 22) and $M=5$ (Fig. 23)) is that the waveform in Fig. 35 involves significant elongation of the cross-section perimeter and therefore becomes rather stiff.

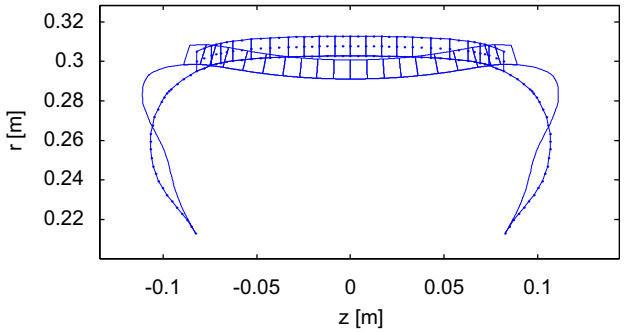

Fig. 36. Cross-section mode corresponding to $\kappa=0$ and $f=408$ Hz (symbol '◀' in Fig. 13 (a)).

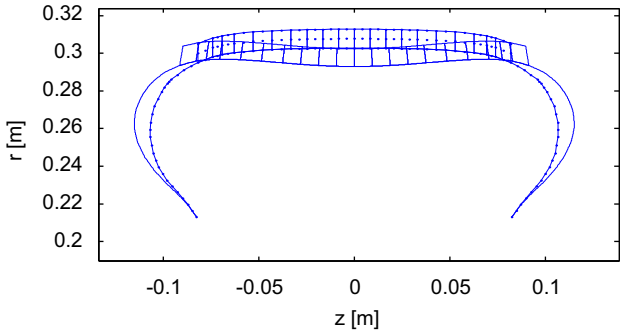

Fig. 37. Cross-section mode corresponding to $\kappa=1$ and $f=496$ Hz (symbol '◀' in Fig. 13 (a)).

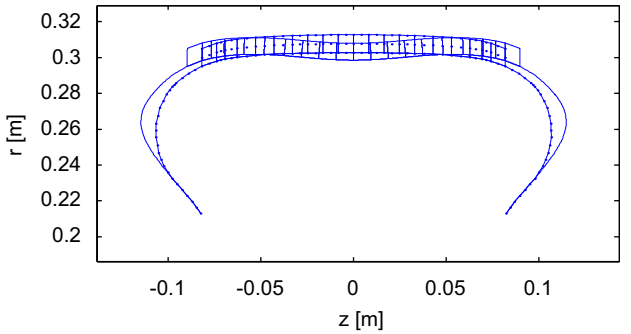

Fig. 38. Cross-section mode corresponding to $\kappa=2$ and $f=639$ Hz (symbol '◀' in Fig. 13 (a)).

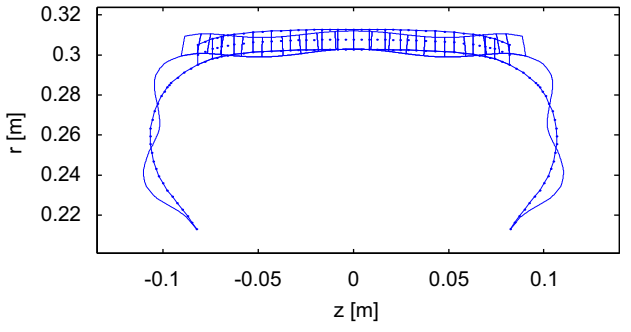

Fig. 39. Cross-section mode corresponding to $\kappa=3$ and $f=729$ Hz (symbol '◀' in Fig. 13 (a)).

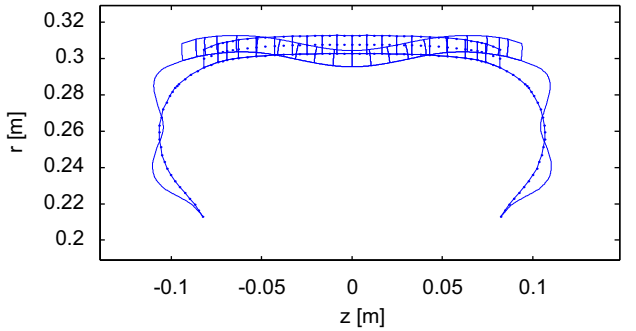

Fig. 40. Cross-section mode corresponding to $\kappa=4$ and $f=822$ Hz (symbol '◀' in Fig. 13 (a)).

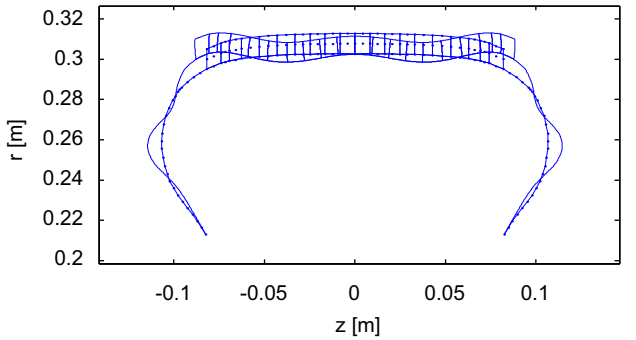

Fig. 41. Cross-section mode corresponding to $\kappa=5$ and $f=987$ Hz (symbol '◀' in Fig. 13 (a)).

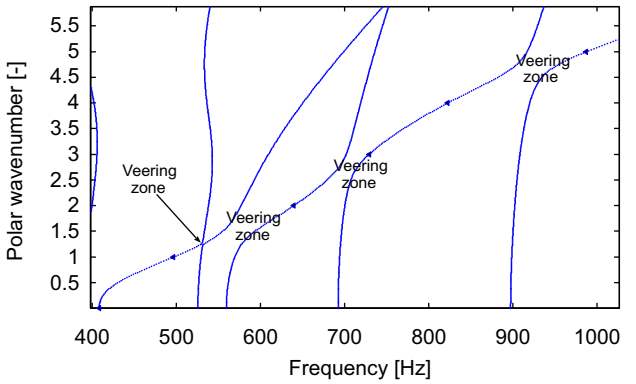

Fig. 42. Dispersion relations, in a limited frequency–wavenumber range, for symmetric wave-forms.

• In Fig. 16, at frequencies above 400 Hz, it is noted that in addition to the symmetric belt bending modes, another set of modes are possible to distinguish, located along an approximately straight line. These modes, corresponding to the symbol '◀' in Fig. 13 (a), are more clearly manifested in Figs. 14 and 15. By inspecting the corresponding cross-section vibration patterns, Figs. 36–41, it is concluded that the belt generally exhibits substantial extensional (or elongation) deformation. However, besides this common feature, the cross-section modes are essentially different. In order to illustrate the behaviour more closely, consider Figs. 42 and 43.

In Fig. 42, a close-up of the dispersion relations is given in a small region around the modes under discussion. For clarity, a refined wavenumber resolution has been used and only waves with symmetric cross-section modes are depicted. As seen, at 408 Hz a wave cuts on with cross-section mode according to Fig. 36. As the corresponding branch evolves over frequency, a gradual change in waveform occurs and as the polar wavenumber reaches $\kappa=1$, the waveform has the appearance given in Fig. 37. As this branch evolves further, a point is reached at which it attempts to cross the branch cutting on at 525 Hz. However, if the region around this apparent crossing is magnified, it is seen that the dispersion

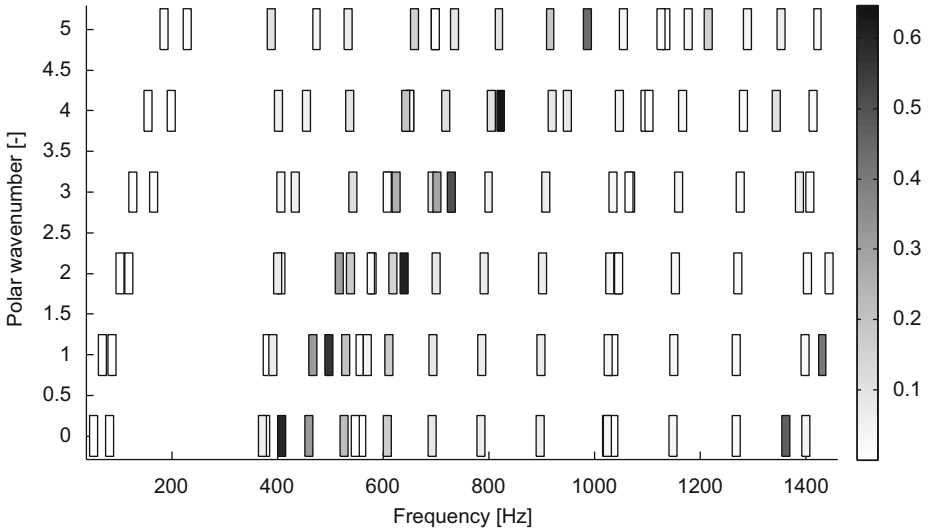

Fig. 43. Portion of total strain energy which is due to extensional deformation of the central belt region.

branches do not cross, but instead veer away from each other. This phenomenon, referred to as 'curve veering' or 'attempted crossings' [31], occurs if two dispersion branches with non-orthogonal waveforms attempt to cross. At increasing frequency, as seen in Fig. 42, additional veering zones are observed and by inspecting the cross-section modes around each zone it is noted that, in general, these zones introduce a substantial change in the appearance of the waveform belonging to the belt extensional wave. Additional, gradual, changes in cross-section mode occur in between the veering zones. Thus, the substantial changes in waveform observed in Figs. 36–41 are explained partly by veering and partly by gradual changes in between the veering zones.

To explain Fig. 43, consider, to start with, a 3-D mode on the tyre (for example that is depicted in Fig. 19) and assume that the vibration field is given by this mode only. For this 'mono-mode' motion, the total strain energy stored in the tyre can be computed, if a certain amplitude is assumed for the mode under study. This strain energy, denoted by $E^{\mathrm{tot}}_{\mathrm{strain}}$ in the following, is given by summing up the contributions from all (shell as well as solid) elements in the model (this is indicated by the superscript 'tot' used above, denoting 'total, when summed over all elements'). Considering the strain energy belonging to one individual shell element, this energy can be further decomposed into several contributions corresponding to different types of deformation (for example extensional deformation, in-plane shearing, shearing across the element thickness, etc.[1]). Fig. 43 depicts, for each 3-D mode having ≤ 5 wavelengths around the circumference, the following quotient:

$$\alpha = \frac{E^{\text{ext, motion of shell el 19}-28}_{\mathrm{strain}}}{E^{\mathrm{tot}}_{\mathrm{strain}}} \tag{5}$$

This quotient (which is independent of the amplitude assigned to the mode under study), gives the portion of the total strain energy which is due to extensional motion of the shell elements numbered from 19 to 28. These elements, located within the range $|z| \leq 0.043$ m in Fig. 3, are referred to as the 'central belt region' henceforth. As seen, the 3-D modes addressed in this paragraph (the ones with cross-section motion according to Figs. 36–41) are strongly manifested in Fig. 43, with more than half of the strain energy being due to extensional deformation of the central belt region. If a region considerably smaller or larger than $|z| \leq 0.043$ m is considered, the addressed modes become less dominant. Thus, the motivation for considering this specific range is to show how these modes distinguish themselves as compared to the remaining modes. As a last note regarding Fig. 43, it is observed that the κ=0 and 1 modes corresponding to the wave cutting on at 1363 Hz (that with a 'breathing' motion at the cross-section plane, Fig. 35), are also well manifested in this figure.

In summary, the different wave-types found in the high-frequency region involve belt bending waves ('▲' and '▼'), sidewall waves of the in-plane type ('○', '+', '|' and '▶') and of the out-of-plane type ('◇' and '□'), a wave with significant extensional deformation of the central belt region ('◀') and a wave for which the cross-section mode exhibits a breathing motion ('⌂'). Generally, the dispersion properties are more complex than in the low-frequency range, involving phenomena such as 'curve veering' and waves for which the phase speed and group speed have opposite signs.

[1] For an element without pretension, these contributions are found from Eqs. (73), (64) and (76) in [20]. If an element with pretension is considered, as in the present work, an additional term will enter into the integrand in Eq. (73), taking into account the strain energy induced by static pretension forces.

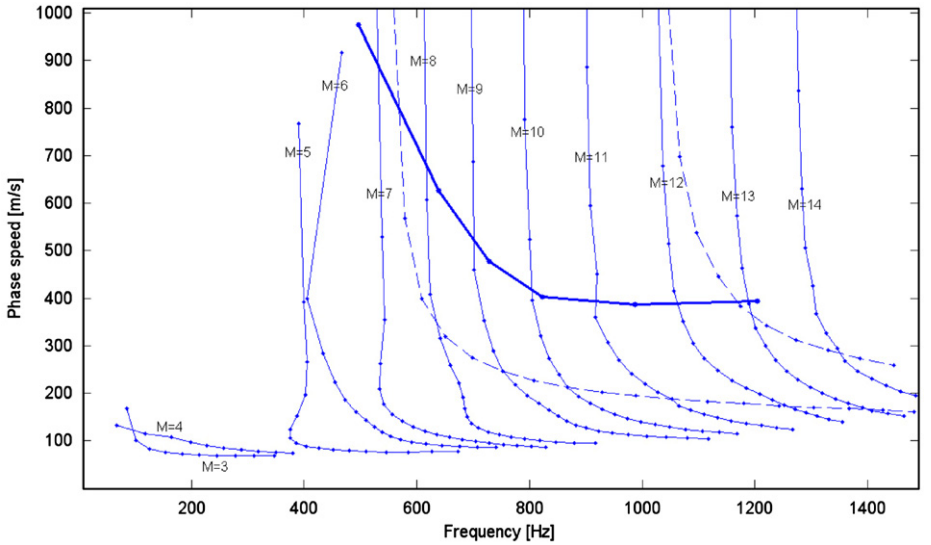

Fig. 44. Phase speed of waves belonging to Group I (thin lines), Group II (thick line) and Group III (dashed lines). Concerning Group II, only the wave with symbol '◀' in Fig. 13 (a) is depicted. The other wave belonging to this group (marked '⌂' in Fig. 13 (a)), cuts on at the end of the frequency range considered and is therefore not shown above. Further, the *M* attached to each thin line is the number of half-wavelengths of out-of-plane displacement along the lateral direction (see sub-section 4.2, first paragraph). Finally, since each symmetric wave within Group III has a phase speed almost identical to that of its anti-symmetric 'neighbour', only the symmetric waves are depicted above.

5. Discussion and conclusions

A tyre model based on waveguide finite elements, originally presented in [6, Paper A], has been implemented using input data provided by Continental. Simulated point and transfer mobilities have been compared to the corresponding measured quantities, showing a very good agreement. The model has been used to investigate (in the frequency range 0–1500 Hz) the wave content on a tyre that is (A) stationary and (B) not making contact with the ground.

Previous measurements of the phase speed on tyres, as well as work with simplified models, resulted in a description of the wave content by mainly two wave types: Waves with a strong radial component and in-plane waves [1]. The analysis conducted in this paper modifies this picture as follows.

Based on the characteristics of their cross-section modes, the waves on a stationary tyre, not in contact with the ground, can be grouped (roughly) into three categories. Waves belonging to the first category, Group I, have cross-section modes involving strong out-of-plane motion and correspond to the symbols '⊥', '×', '▲' and '▼' in Fig. 13 (a and b). The phase speeds corresponding to this group, depicted in Fig. 44, are in fairly good agreement with the measured results presented in [1]. As seen, the phase speed is relatively low and increases from about 70 to 100 ms^{-1} in the range 200–1500 Hz. For high enough wavenumbers, the cross-section modes change into waveforms characterized by large sidewall deformation (symbols '◇' and '□' in Fig. 13 (a)), as described in sub-section 4.2.

The second category, Group II, is constituted by waves involving significant extensional deformation of either the whole cross-section, '⌂', or the central belt region, '◀'. The latter wave ('◀') cuts on at about 400 Hz and its waveform evolves over frequency as depicted in Figs. 36–41. From Fig. 44, the phase speed is seen to be relatively high, approaching some 400 ms^{-1} for high-order κ. The former wave ('⌂') is also expected to have a rather high phase speed, although this cannot be confirmed without extending the frequency range in Fig. 13 (a) to considerably higher frequencies.

The third category, Group III, concerns waves with strong in-plane motion of the sidewalls and rather weak out-of-plane motion of the belt ('○', '+', '|' and '▶'). The phase speed is determined by the Young's modulus of the sidewalls, which is substantially smaller than the combined stiffness of the belt and tread. As seen in Fig. 44, the phase speed is in the order of 200 ms^{-1}.

Concerning sound radiation one can conclude that Group I has a rather low wave speed. In addition, lateral cancellation effects will lead to rather weak radiation. Group III has a higher phase speed, but very low response in the normal direction to the tyre surface. The waves belonging to Group II would be much better radiators, due to their high phase speed (although lateral cancellation will occur for high-order modes corresponding to the '◀'-marked wave). In particular, the wave with a 'breathing' motion at the cross-section plane, see Fig. 35, is likely to radiate efficiently, since this waveform acts as a pure volume source.

This view is certainly correct for a tyre excited by a point force, radiating into free-field. For a rolling tyre, however, the situation might change substantially. Firstly, the so-called horn effect will lead to different radiation conditions along

the circumference of the tyre. Secondly, lateral cancellation effects might be prevented due to the contact patch. Thirdly, the question arises which waves are actually excited during rolling.

In general, the sound radiation from a structure does not depend only on the properties of free waves, but also on the type of excitation. Excitations with different spatial distributions will lead to different modal compositions of the vibration field on the structure. This means that without taking into account the correct excitation during rolling, it is not possible to say which modes are responsible for sound radiation from a rolling tyre. To investigate this question will be the subject of future publications.

References

[1] W. Kropp, Structure borne sound on a smooth tyre, *Applied Acoustics* 26 (1989) 181–192.
[2] P. Andersson, K. Larsson, F. Wullens W. Kropp, High frequency dynamic behavior of smooth and patterned passenger car tyres, *Acta Acustica united with Acustica* 90 (2004) 445–456.
[3] Y.J. Kim, J.S. Bolton, *Modelling tyre treadband vibration*, Internoise, The Hague, 2001.
[4] W. Kropp, F.X. Becot, S. Barrelet, On the sound radiation from tyres, *Acta Acustica united with Acustica* 86 (2000) 769–779.
[5] F. Wullens, W. Kropp, Wave content of the vibration field of a rolling tyre, *Acta Acustica united with Acustica* 93 (2007) 48–56.
[6] M. Fraggstedt, Power dissipation in car tyres, licentiate thesis, Department of Aeronautical and Vehicle Engineering, Royal Institute of Technology, 2006. Available at: 〈http://www.ave.kth.se/publications/mwl/downloads/TRITA-AVE_2006-26.pdf〉.
[7] F. Böhm, Mechanik der Gurtelreifens, *Ingenieur Archiv* 35 (1966) 82–101.
[8] W. Kropp, Ein Modell zur Beschreibung des Rollgeräusches eines unprofilierten Gurtelreifens auf rauher Straβenoberfläche (A model for describing the rolling noise from a smooth tyre on a rough road surface), doctoral thesis, Fortschrittberichte VDI, Reihe 11: Schwingungstechnik, no. 166, 1992.
[9] J.M. Muggleton, B.R. Mace, M.J. Brennan, Vibrational response prediction of a pneumatic tyre using an orthotropic two-plate model, *Journal of Sound and Vibration* 264 (2003) 929–950.
[10] K. Larsson, W. Kropp, A high frequency three-dimensional tyre model based on two coupled elastic layers, *Journal of Sound and Vibration* 253 (2002) 889–908.
[11] P. Andersson, K. Larsson, Validation of a high frequency tyre model based on the elastic field equations, 10th International Congress on Sound and Vibration, Stockholm, 2003.
[12] L.E. Kung, W. Soedel, T.Y. Yang, Free vibration of a pneumatic tyre–wheel unit using a ring on an elastic foundation and a finite element model, *Journal of Sound and Vibration* 107 (1986) 181–194.
[13] T.L. Richards, Finite element analysis of structural–acoustic coupling in tyres, *Journal of Sound and Vibration* 149 (1991) 235–243.
[14] A. Pietrzyk, *Prediction of the dynamic response of a tyre*, Internoise, The Hague, 2001.
[15] A. Fadavi, D. Duhamel, H.P. Yin, *Tyre/road noise: Finite element modelling of tyre vibrations*, Internoise, The Hague, 2001.
[16] M. Brinkmeier, U. Nackenhorst, S. Petersen, O. von Estorff, A finite element approach for the simulation of tire rolling noise, *Journal of Sound and Vibration* 309 (2008) 20–39.
[17] I. Lopez, R.E.A. Blom, N.B. Roozen, H. Nijmeijer, Modelling vibrations on deformed rolling tyres—a modal approach, *Journal of Sound and Vibration* 307 (2007) 481–494.
[18] Y. Waki, B.R. Mace, M.J. Brennan, Free and forced vibrations of a tyre using a wave/finite element approach, *Journal of Sound and Vibration* 323 (2009) 737–756.
[19] C. M. Nilsson, Waveguide finite elements applied on a car tyre, doctoral thesis, Department of Aeronautical and Vehicle Engineering, Royal Institute of Technology, 2004. Available at: 〈http://www.flyg.kth.se/staff/mwl/downloads/C_M_Nilsson_PhD_Thesis.pdf〉.
[20] S. Finnveden, M. Fraggstedt, Waveguide finite elements for curved structures, *Journal of Sound and Vibration* 312 (2008) 644–671.
[21] B. Aalami, Waves in prismatic guides of arbitrary cross section, *Journal of Applied Mechanics* 40 (1973) 1067–1071.
[22] L. Gavric, Computation of propagative waves in a free rail using a finite element technique, *Journal of Sound and Vibration* 184 (1995) 531–543.
[23] L. Gavric, Finite element computation of dispersion properties of thin walled waveguides, *Journal of Sound and Vibration* 173 (1994) 113–124.
[24] U. Orrenius, S. Finnveden, Calculation of wave propagation in rib-stiffened plate structures, *Journal of Sound and Vibration* 198 (1996) 203–224.
[25] C.M. Nilsson, S. Finnveden, Waves in thin-walled fluid filled ducts with arbitrary cross-section, *Journal of Sound and Vibration* 310 (2008) 58–76.
[26] S. Finnveden, Evaluation of modal density and group velocity by a finite element method, *Journal of Sound and Vibration* 273 (2004) 51–75.
[27] F. Birgersson, S. Finnveden, C.M. Nilsson, A spectral super element for modelling of plate vibration. Part 1: General theory, *Journal of Sound and Vibration* 287 (2005) 297–314.
[28] W. Kropp, Technical Acoustics 1', Educational script, Department of Applied Acoustics, Chalmers University of Technology, 2001. Obtain this reference as a PDF file, by sending an e-mail to the corresponding author.
[29] E. Rustighi, S.J. Elliott, S. Finnveden, K. Gulyas, T. Mocsai, M. Danti, Linear stochastic evaluation of tyre vibration due to tyre/road excitation, *Journal of Sound and Vibration* 310 (2008) 1112–1127.
[30] A. Pietrzyk, J. Leyssens, A. Lerusse, *FE modelling for tyre noise*, Euronoise, Naples, 2003.
[31] N.C. Perkins, C.D. Mote, Comments on curve veering in eigenvalue problems, *Journal of Sound and Vibration* 106 (1986) 451–463.